AIAA Propulsion and Energy Forum
19-22 August 2019, Indianapolis, IN
AIAA Propulsion and Energy 2019 Forum

10.2514/6.2019-4175

Numerical investigation of Non-Synchronous Vibration using Scale Adaptive Simulation turbulence model

Purvic Patel* and Hong-Sik Im† and Gecheng Zha‡
Dept. of Mechanical and Aerospace Engineering
University of Miami, Coral Gables, Florida 33124
E-mail: gzha@miami.edu

The Non-Synchronous Vibration simulation is carried out for the GE 1-1/2 stage high speed compressor using a hybrid turbulence model. The Scale Adaptive Simulation (SAS) version of Spalart-Allmaras (SA) hybrid turbulence model is used with the Low Diffusion E-CUSP Riemann solver. A 3rd order WENO scheme for the inviscid flux and a 2nd order central differencing scheme for the viscous flux are used in the present study. The predicted NSV frequency is compared with the experimentally measured. The counter rotating tip vortex instability is found to trigger the non-engine order large amplitude vibration. The predicted frequency with the present hybrid turbulence model agrees well with the rig test results.

I. Nomenclature

L_{ref}	=	Reference length
ρ_∞	=	Freestream density
U_∞	=	Freestream velocity
μ_∞	=	Freestream dynamics viscosity
$\mathbf{\Omega}$	=	Vorticity
Re	=	Reynolds number
i	=	Dummy indices for Indicial / Einstein summation notation
κ	=	von-Karman constant
$l,\ m,\ n$	=	Elemental surface normal vector in ξ, η and ζ directions
$U,\ V,\ W$	=	Contravariant velocities in ξ, η and ζ directions
Δq	=	Difference between the velocity at the field point and that at the trip (on the wall)
Δx_t	=	Grid spacing along the wall at the trip
ω_t	=	Wall vorticity at the trip
d_w	=	Distance from the nearest wall gridpoint
d_t	=	Distance from the field point to the trip
SA-noft2	=	Spalart-Allmaras One-Equation Model without f_{t2} Term
LES	=	Large Eddy Simulation
DES	=	Detached-Eddy Simulation
DDES	=	Delayed Detached-Eddy Simulation
SAS	=	Scale Adaptive Simulation
NSV	=	Non-Synchronous Vibration
SFV	=	Separated Flow Vibration
WENO	=	Weighted Essentially Non-Oscillatory
CUSP	=	Convective Upwind and Splitting Pressure

*Ph.D. Candidate
†Ph.D., Currently working at Doosan ATS America
‡Professor, ASME Fellow, AIAA associate Fellow.

II. Introduction

Blade vibrations are one of the primary focus areas of all turbomachinery designers, as high amplitude vibrations can lead to the complete breakdown of an engine. These vibrations causing the aero-elastic phenomena in blades are broadly classified into the forced response and flutter. Both phenomena, occuring at the natural frequency of a blade, have been investigated till now extensively. The forced response excitation of the rotor blades arises from aerodynamic excitations such as inlet flow distortion, and upstream wakes. To drive the forced response excitation, almost all of these sources except those from rotating stall, must be at harmonics of the rotational frequency of the rotor itself [1]. In case of a flutter, a self-excited vibration, rotor blades vibrate at a natural frequency due to insufficient mechanical damping to overcome the vibrations.

Another turbomachinery aeromechanics problem, namely non-synchronous vibration (NSV), has gained a lot of attention over the last two decades. A non-synchronous vibration occurs in the stable operating range of the compressor. In this non-engine order excitation, a large amplitude vibration occurs due to the complex flow phenomenon such as rotating instability (RI) [2–9] and circumferentially traveling vortices in the tip region. Here, the frequency response is not necessarily the blade natural frequency [5]. At NSV, blades experience High Cycle Fatigue (HCF) with Limit Cycle Oscillation (LCO), which can lead to the premature blade failure. With the experimental analysis of a 10 stage high speed compressor, Baumgartner et al. [2] have shown that the first stage rotor experiences high amplitude NSV vibrations due to the rotating flow instability in the blade tip region for a certain operating condition. Mailach et al. [3] carried out experimental investigations of rotating instabilities in a four stage compressor with inlet guide vane. Based on their experiments, the periodic interaction of one blade tip vortex with the adjacent blade flow generates RIs near the stability limit of the compressor with a relatively large tip clearance. Another experimental and numerical analysis, on a low-speed single-stage fan with outlet guide vanes by März et al. [4], has found the NSV of roughly half the blade passing frequency (BPF) at high load operating condition due to the tip flow instability.

Thomassin et al. [10] proposed the jet core feedback theory to explain a physical mechanism behind the NSV. Based on their theory, an acoustic reflection is produced when the jet core impinges on a rigid plate. When the wavelength of this reflection matches with the jet-to-plate distance, the resonance jet condition arises which creates a significant amplification of the pressure unsteadiness on the plate. In order to validate their proposed mechanism, Thomassin et al. [6] conducted an experiment on a compressor consisting of a high pressure compressor first stage rotor and deswirl vanes. A criterion for resonance condition based on their theory appears to be in good agreement with experimental data.

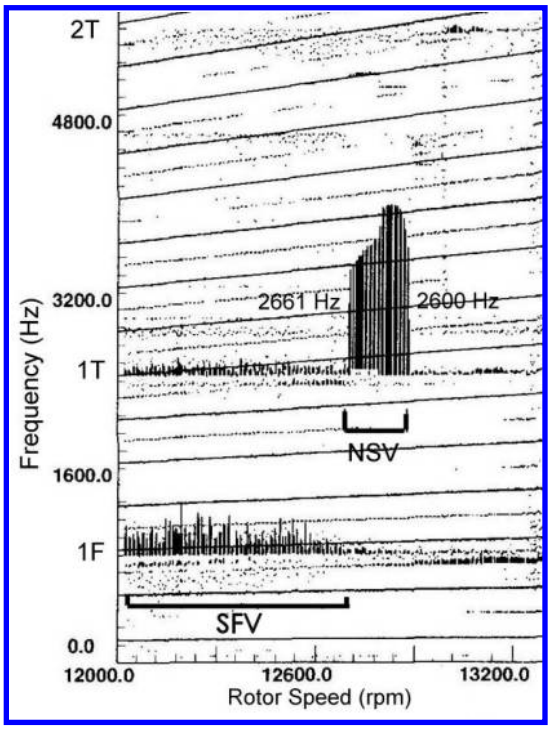

Figure 1 Strain gauge response of first stage rotor blades in a rig test [5]

Computational Fluid Dynamics (CFD) is a very useful numerical analysis tool for understanding the underlying mechanism behind the NSV. An unsteady RANS (URANS) model is overly diffusive in nature, and can not provide the flow details like the Large Eddy Simulation (LES) or a hybrid turbulence model, it also fails to provide quantitative and qualitative aerodynamic prediction with large flow separation [23]. The LES can overcome many shortcomings of URANS, however for high Reynolds number flows it requires computational resources similar to Direct Numerical Simulation (DNS) to resolve the wall boundary layer. This impairs the use of LES for many industrial high Reynolds number applications. A hybrid turbulence model is a compromise between URANS and LES. It uses the URANS near the wall and the LES away from the wall. Thereby it overcomes the need of highly refined mesh near the wall by the LES. Over the last two decades, a hybrid turbulence model has fetched a lot of attention in the research community to investigate highly separated flow and it is found to be promising. As tip flow instability is responsible for the NSV, a high-fidelity simulation using the hybrid turbulence model can provide in-depth flow details with improved quantitative and qualitative results.

Fig. 1 shows a strain gauge response of GE 1-1/2 high speed compressor first stage rotor blades with a tip clearance of $1.1\,\%$ tip axial chord. A step change in the NSV frequency in the range from $2661\,\mathrm{Hz}$ to $2600\,\mathrm{Hz}$ is observed in a rig test with the increase in rotational speed of compressor from $12{,}700\,\mathrm{rpm}$ to $12{,}880\,\mathrm{rpm}$. Kielb et al. [5] have carried out numerical investigation of the NSV using the URANS model on the 1/7th annulus sector of its rotor row. Based on their simulation, the NSV is caused by the vortex unsteadiness on the suction side near $75\,\%$ span and the tip flow oscillation near the leading edge. Their predicted frequency is approximately $9\,\%$ lower than the rig test. Im et al. [8] have also carried out numerical investigation of the same 1/7th annulus sector of GE 1-1/2 stage compressor with inlet guide vanes and stator vanes using the URANS. In their results, the NSV frequency is under-predicted by $3.3\,\%$. In another numerical investigation by Im et al. [9], they used the Delayed Detached Eddy Simulation (DDES) based on Spalart-Allmaras (SA) turbulence model for the same. With this hybrid turbulence model, their predicted NSV frequency is $14.7\,\%$ lower than the experimental results. Based on their results, this under-prediction is attributed to the tendency of DDES to predict rotor stall earlier than the URANS and the NSV can be achieved only at higher mass flow rate, which generates a lower frequency [9].

In the present study, the Scale Adaptive Simulation (SAS) based on the SA turbulence model [23] is used to investigate the NSV mechanism for the GE 1-1/2 stage high speed compressor. This hybrid turbulence model doesn't suffer from the Modeled Stress Depletion (MSD) problem seen with the Delayed Detached Eddy Simulations (DDES) version of SA hybrid turbulence model. This motivates the present study to investigate the compressor NSV phenomenon with the SA-SAS hybrid turbulence model and to study the mechanism behind the NSV.

III. Turbulence model

In the present work, spatially filtered compressible Navier-Stokes equations along with the SA based SAS turbulence model are solved in fully coupled manner in a rotating frame using an implicit unfactored Gauss-Seidel line iteration to achieve high convergence rate [11]. These equations are nondimensionalized using L_{ref}, ρ_∞, U_∞ and μ_∞. In the SA-SAS turbulence model, the transport equation for the modified eddy viscosity ($\hat{\nu}$) in generalized coordinates using the indicial notation is given by:

$$\frac{\partial \rho\hat{\nu}}{\partial t} + \frac{\partial \rho\hat{\nu}U_i}{\partial \xi_i} = \frac{1}{Re}\left[\frac{\partial}{\partial \xi}\left(\frac{\rho}{\sigma}\left(\nu+\tilde{\nu}\right)\frac{\partial \tilde{\nu}}{\partial x_i}l_i\right) + \frac{\partial}{\partial \eta}\left(\frac{\rho}{\sigma}\left(\nu+\tilde{\nu}\right)\frac{\partial \tilde{\nu}}{\partial x_i}m_i\right) + \frac{\partial}{\partial \zeta}\left(\frac{\rho}{\sigma}\left(\nu+\tilde{\nu}\right)\frac{\partial \tilde{\nu}}{\partial x_i}n_i\right)\right] + S_v \quad (1)$$

where,

$$S_v = \frac{1}{J}\left[\rho c_{b1}\left(1-f_{t2}\right)\hat{S}\hat{\nu} - \frac{1}{Re}\left(\rho\left(c_{w1}f_w - \frac{c_{b1}}{\kappa^2}f_{t2}\right)\left(\frac{\hat{\nu}}{d_w}\right)^2\right) + Re\left(\rho f_{t1}\left(\Delta q\right)^2\right) + \frac{1}{Re}\frac{\rho}{\sigma}c_{b2}\frac{\partial \hat{\nu}}{\partial x_i}\frac{\partial \hat{\nu}}{\partial x_i}\right] \quad (2)$$

The turbulent eddy viscosity (μ_{SAS}) is calculated from the modified eddy viscosity ($\hat{\nu}$) using the relation

$$\mu_{SAS} = \rho\hat{\nu}f_{v1} \quad (3)$$

The auxiliary relations used to calculate various terms appearing in Eqs. (2) and (3) are:

$$\begin{aligned}
&\chi = \frac{\hat{\nu}}{\nu}\,, && f_{v1} = \frac{\chi^3}{\chi^3 + c_{v1}^3}\,, && f_{v2} = 1 - \frac{\chi}{1 + \chi f_{v1}} \\
&\hat{S} = \Omega + \overline{S}\,, && \overline{S} = \frac{1}{Re}\frac{\hat{\nu}}{\kappa^2 d_w^2} f_{v2}\,, && g = r + c_{w2}r^6 - r \\
&f_w = g\left(\frac{1 + c_{w3}^6}{g^6 + c_{w3}^6}\right)^{16}\,, && r = min\left(\frac{\hat{\nu}}{\hat{S}\kappa^2 d_w^2}, 10\right)\,, && f_{t2} = c_{t3}\exp\left(-c_{t4}\chi^2\right) \\
&f_{t1} = c_{t1} g_t \exp\left[-c_{t2}\frac{\omega_t^2}{\Delta U^2}\left(d^2 + g_t^2 d_t^2\right)\right]\,, && g_t = min\left(0.1, \frac{\Delta q}{\omega_t \Delta x_t}\right)
\end{aligned} \tag{4}$$

Constants used in Eqs. (1), (2) and (4) are:

$$\begin{aligned}
&c_{b1} = 0.1355\,, && \sigma = \frac{2}{3}\,, && c_{b2} = 0.622\,, && \kappa = 0.41 \\
&c_{w2} = 0.3\,, && c_{w3} = 2\,, && c_{v1} = 7.1\,, && c_{t3} = 1.1 \\
&c_{t4} = 2.0\,, && c_{w1} = \frac{c_{b1}}{\kappa^2} + \frac{1 + c_{b2}}{\sigma}\,, && c_{t1} = 1.0\,, && c_{t2} = 2.0
\end{aligned} \tag{5}$$

In the current study, the fully turbulent flow assumption allows the term f_{t2} and the trip term (f_{t1}) to assume zero value. This makes the turbulence model equation of the form SA-noft2. Details of the standard SA turbulence model implementation in a rotating frame can be found in reference [12]. In order to avoid numerical difficulties arising from the zero or negative value of $\hat{S}$, modifications suggested by Allmaras et al. [13, 14] are incorporated in the Eq. (4) and the same is given by:

$$\hat{S} = \begin{cases} \Omega + \overline{S} & : \overline{S} \geq -c_2\Omega \\ \Omega + \frac{\Omega c_2^2 \Omega + c_3 \overline{S}}{c_3 - 2c_2\Omega - \overline{S}} & : \overline{S} < -c_2\Omega \end{cases} \tag{6}$$

where, $c_2 = 0.7$, $c_3 = 0.9$ and set $r = 10$ if $\hat{S} = 0$.

A. SA-SAS turbulence model

In 1997, Spalart et al. [15] proposed Detached Eddy Simulation (DES), a hybrid RANS/LES turbulence model, based on the one equation Spalart-Allmaras (SA) turbulence model. This model is commonly referred as DES97 in the research community. Here, a switch from the RANS to the LES is designed based on the local grid size information. This explicit grid size dependence for different modes creates premature transition to the LES mode within a boundary layer thickness when a wall parallel grid spacing falls below the boundary layer thickness. This leads to a reduction in eddy viscosity and thereby modeled Reynolds stress [16, 17]. However, this modeled Reynolds stress is reduced below the RANS level and the resolved Reynolds stresses arising from the LES is not strong enough to restore the modeled Reynolds stress of the RANS. This Modeled Stress Depletion (MSD) leads to the Grid Induced Separation [16].

In an alternative approach to the DES, Menter et al. [18] developed the KE1E one-equation model for the eddy-viscosity, which is an improved URANS method providing the LES like behavior in detached flow regions. In their derivation, they noticed that the destruction term of the turbulence model relies on the von Karman length scale [19] and not on the distance away from the wall. This length scale allows the model to adjust dynamically to the resolved stresses and provides the LES like behavior in separated flow regions without an explicit grid dependence. This concept is coined as Scale-Adaptive-Simulation [18]. Later in 2004, Menter et al. [20] presented two equation turbulence model $k - \nu_t$ operating in the RANS and SAS mode. The same concept is extended later to the SST two equation turbulence model using ω as second length scale. Recently, the same concept is extended to the SA turbulence model. Xu et al. [21] modify the distance term appearing in the destruction term whereas Coder [22] provides SAS capability to the original SA turbulence model by introducing an additional destruction term relying on the von Karman length scale. In the present SAS implementation, the distance term appearing in destruction term is modified similar to the implementation of Xu et al. However, the strain rate is used as first order velocity gradient here as compared to Xu et al.s' implementation. Patel et al. have implemented SA-SAS turbulence model and validated its capability under the massive flow separation which can be found in the reference [23].

A length scale (L_{vk}) is similar to the mixing length based on von Karman's similarity hypothesis, where the mixing length depends on the velocity distribution instead of its magnitude [24]. A modified length scale (d_w) in Eq. (2) is given by:

$$L_{vk} = \kappa \left| \frac{S}{\sqrt{\frac{\partial^2 u_i}{\partial x_j \partial x_j} \frac{\partial^2 u_i}{\partial x_m \partial x_m}}} \right| \tag{7}$$

$$d_w = min\left(d_w\,,\, max\left(\frac{L_{vk}}{\kappa}\,,\, C_{des}\Delta_{max}\right)\right) \tag{8}$$

where,

$$S = \sqrt{2S_{ij}S_{ij}} \tag{9}$$

$$S_{ij} = \frac{1}{2}\left(\frac{\partial u_i}{\partial x_j} + \frac{\partial u_j}{\partial x_i}\right) \tag{10}$$

This length scale allows model to adjust dynamically under massive flow separation. In order to avoid singularity for $1L_{vk}$ due to mean-strain rate approaching to zero, DES limiter is introduced in its length scale. This limiter also allows high wave number damping to dissipate the energy to the smallest scale rather than accumulating. With the presence of sufficiently strong instability or initially resolved flow, this model allows the formation of a turbulent spectrum [25]. In a Kolmogorov spectrum, the smallest scales dominate first and second order velocity derivatives, thereby L_{vk} adjusts to the smallest scales to allow the formation of the turbulent spectrum [25].

IV. Computational Set-Up

A. Geometry and mesh description

The full annulus geometry of GE 1-1/2 stage high speed compressor consists of 56 Inlet Guide Vane (IGV) blades, 35 Rotor blades and 70 stator blades. The tip clearance of rotor blade is $1.1\,\%$ of the tip axial chord. In the present study, only 1/7th sector of full annulus is considered with the assumption of 5 Nodal Diameters (ND). O-mesh topology is used around a blade as it ensures highly orthogonal grid near the wall. H-mesh topology is used between row of blades so that the mesh at the stationary and rotating frame interface is one-to-one connected. This also ensures flux the conservation between the different frame of reference. The tip region is fully gridded with 21 grid points. Table 1 provides an overview of number grid points in the direction around the blade (i), blade to blade (j) and spanwise (k), respectively for all blades. The total mesh size of 1/7th sector geometry under consideration is $11{,}886{,}560$. The mesh refinement study was not considered in present study, as this mesh is used earlier for the NSV study by Im et al. [8, 9].

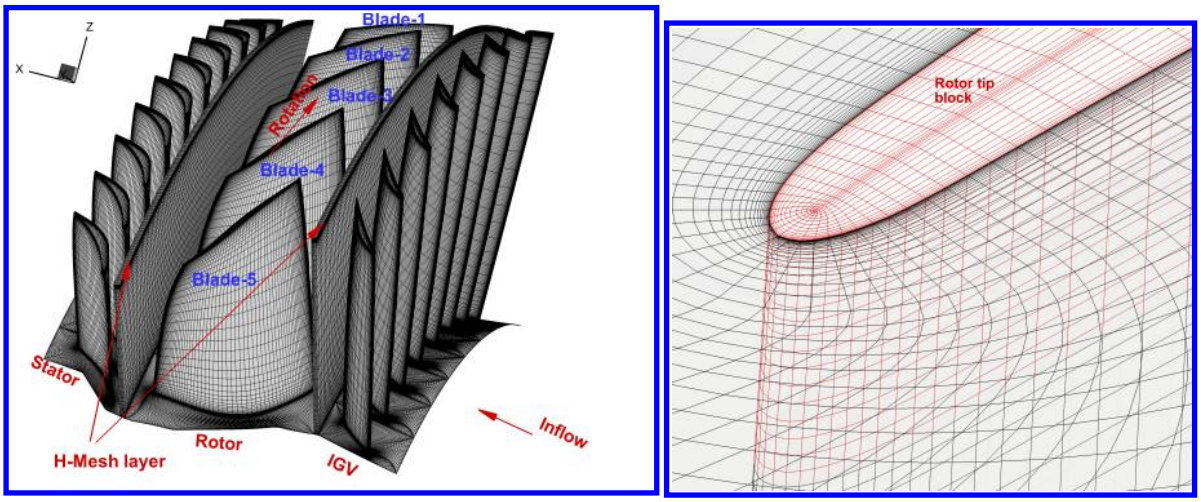

(a) 1/7th Annulus mesh **(b) Rotor tip block mesh**

Figure 2 Mesh overview

Domain	$i \times j \times k$
Rotor blade	$201 \times 51 \times 71$
IGV	$115 \times 51 \times 71$
Stator vane	$121 \times 51 \times 71$

Table 1 Grid points around a blade

B. Boundary Conditions (BCs)

At the IGV inlet, the radial profiles of total pressure, total temperature, swirl angle and pitch angle are defined based on experimental measurements. A velocity component is extracted from the inner domain to determine the rest of flow variables. At the stator outlet, the radial profile of static pressure is defined. Due to the subsonic flow at the stator outlet, remaining flow variables are extracted from the inner domain. At the periodic boundaries, time shifted phase lag boundary condition [26] is applied with the nodal diameter of 5. On the blade surface, no-slip wall boundary condition is defined, whereas the remaining walls are modeled with an efficient wall boundary condition [27], which switches from no-slip wall BC to wall function if y^+ is between 11 to 300. Zero heat flux though the wall is imposed by an adiabatic equation. Fully conservative sliding boundary condition [12] is defined between the blade rows. The compressor operating point used for the current NSV simulation is $2600\,\mathrm{Hz}$ at $12{,}880\,\mathrm{rpm}$.

C. Numerical methods

In the present study, the Low Diffusion E-CUSP (LDE) scheme [28] is used for the inviscid flux evaluation, where the conservative variables at the interface are reconstructed using 3^{rd} order WENO scheme and 2^{nd} order central differencing scheme is used for the viscous flux calculation. An implicit dual time stepping method [29] is used for the temporal terms in 3-D Navier Stokes equation. In each physical time step, the residual is reduced by two orders of magnitude, which is usually achieved within 30 to 35 pseudo time step iterations. A non-dimensional time step of about 0.005 is used. The unsteady simulation is started from the converged steady state result, which is obtained using the mixing plane interface between blade rows. Unsteady simulation with the SA-SAS hybrid turbulence model is carried out for total 13 Revolutions. In order to save the wall clock time, high-scalability parallel computing is used [30].

V. Results and Discussion

A. Campbell diagram

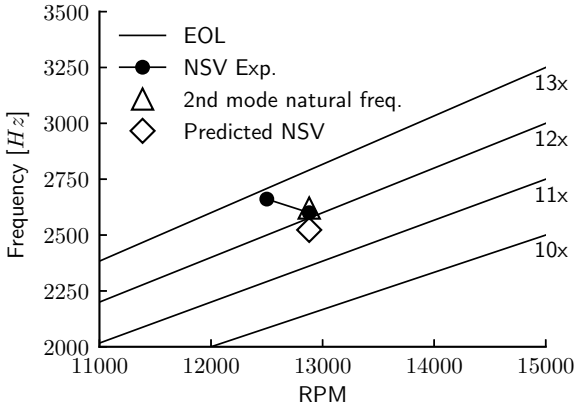

Figure 3 Campbell Diagram

The Campbell diagram with different engine order lines is shown in Fig. 3. It can be seen that the measured NSV frequencies, at different operating speeds in the rig test, remain between the 12th and 13th engine order lines. At 12,880 RPM, the measured NSV frequency is close to the 2nd mode natural frequency (i.e.1st torsional mode frequency). In the present study, the SA-SAS hybrid turbulence model under-predicts the NSV frequency by approximately 2.96 %. The predicted NSV frequency of 2523 Hz lies between the 11th and 12th engine order lines in the Campbell diagram.

B. NSV Frequency Analysis

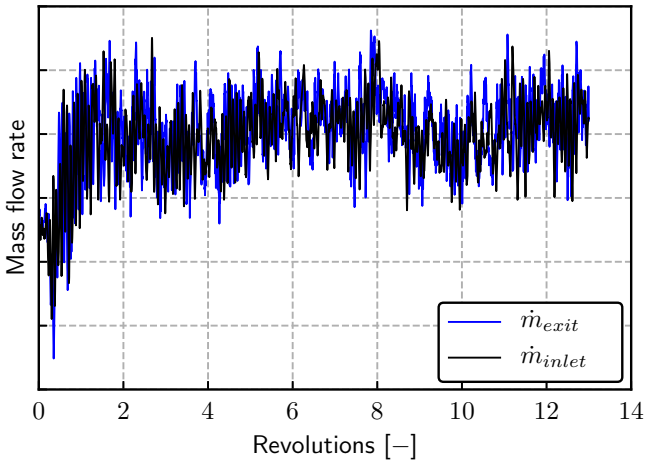

Figure 4 Mass flow rate variation

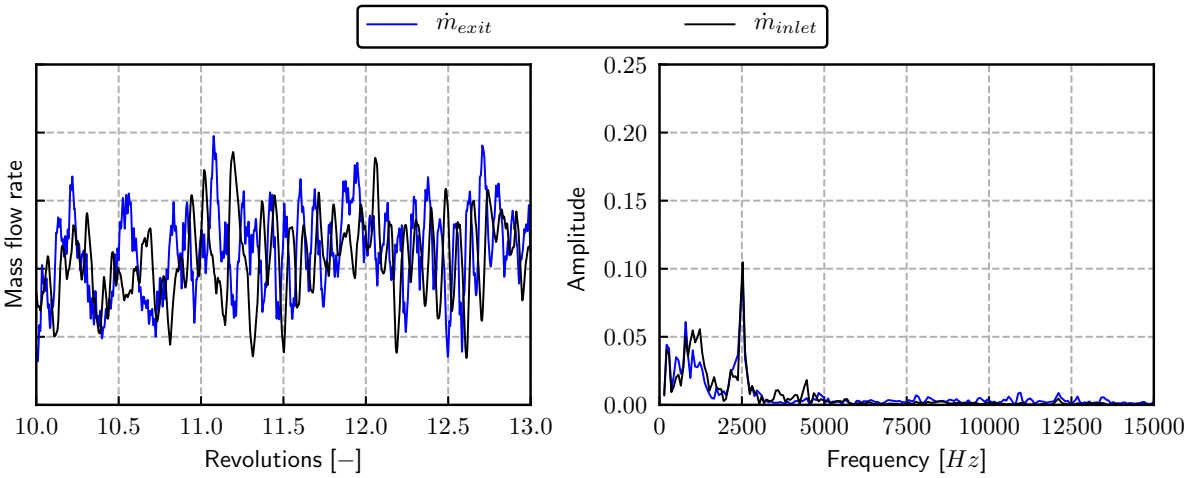

Figure 5 Mass flow rate variation and its frequency analysis

Fig. 4 illustrates the mass flow rate variation as a function of rotor revolutions. For the NSV frequency analysis, initial 10 Revolutions are discarded and the Fast Fourier Transform (FFT) analysis is carried out for the last 3 Revolutions, Fig. 5. Based on the physical mass flow rate, the predicted NSV frequency is 2523 Hz. Based on the exit mass flow rate, another peak is observed near 794 Hz frequency. However, its value and amplitude are observed to be dependent on the FFT sampling rotor revolutions. Similarly, the predicted NSV frequency also varies ± 40 Hz depending on the FFT sampling. The inlet mass flow rate analysis also predicts NSV frequency of 2523 Hz. Apart from this NSV frequency, it

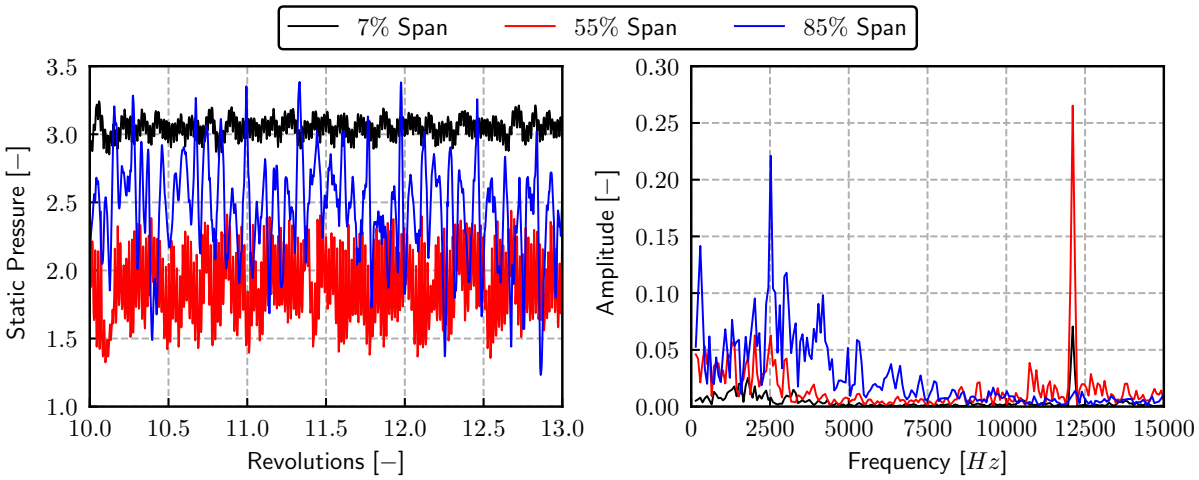

Figure 6 Blade-3 Surface static pressure and its frequency analysis

predicts three peaks at 1225 Hz, 1011 Hz and 794 Hz, which are near the 1^{st} bending mode frequency of 1065.5 Hz. This analysis clearly shows that NSV is not a local blade excitation and it affects the global properties of the entire blade row.

Apart from the frequency analysis based on the physical mass flow rate, normalized blade-3 static pressure at various span locations near the leading edge on the pressure side is also analyzed, Fig. 6. It can be seen that vane passing frequency of IGV (12,118 Hz) is dominant near the mid span as well as near the hub. Near the 85 % span location, NSV frequency of 2523 Hz is dominant and amplitude of vane passing frequency is very low as compared to the other frequencies. Similar to the mass flow rate frequency analysis, the effect of FFT sampling is also observed here. It should be noted that this effect is mostly seen with the use of hybrid turbulence model. In the case of the URANS turbulence model, the amplitude of lower frequency is not as significant as compared to the predicted NSV frequency due to its diffusive nature. As the effect of vane passing frequency decays downstream, the frequency analysis based on the physical mass flow rate does not predict the peak at the vane passing frequency, Fig. 5.

C. Flow Physics

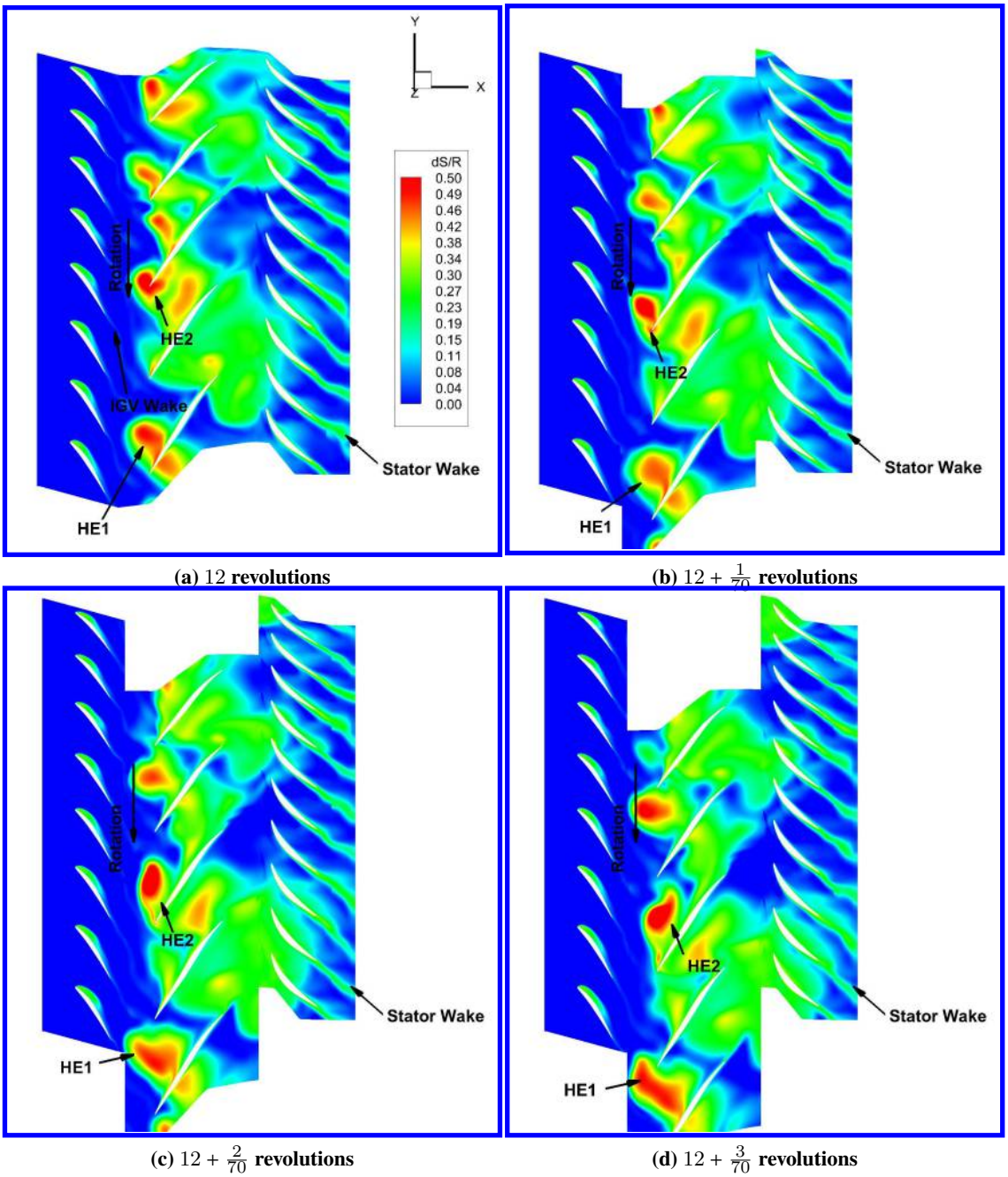

(a) 12 **revolutions** **(b)** $12 + \frac{1}{70}$ **revolutions**

(c) $12 + \frac{2}{70}$ **revolutions** **(d)** $12 + \frac{3}{70}$ **revolutions**

Figure 7 Entropy contours near the $85\,\%$ **span location**

Fig. 7 shows the entropy contour near the $85\,\%$ span location. The high entropy (HE) regions are marked in the figure to understand its traveling pattern in the flow passage. At the start of revolution, HE1 is residing on both suction as well as pressure side of Blade-1 whereas HE2 is located near the leading edge of blade-3. After $\frac{1}{70}$ revolution, the strength of HE1 on the suction side reduces where as on the pressure side it travels circumferentially towards the blade-2 and at the same time it moves downstream along the blade-1 pressure side. Similarly, HE2 is traveling towards blade-4 and at the same time it moves downstream along the blade-3 pressure side. It can also be seen that small high entropy region near the trailing edge of blade-1 is traveling counter rotating direction towards the blade-2 suction side. Due to the vortex shedding from the leading and trailing edge of rotor blade, it experiences the torsional vibration and therefore

the NSV frequency is close to the 1^{st} torsional mode in the present study. This vortex shedding is due to the interaction of the incoming flow, the tip vortex, and the tip leakage flow. With the further $\frac{2}{70}$ and $\frac{3}{70}$ revolutions, HE2 is getting detached from the blade-3 leading edge and travels towards blade-4 leading edge and moving further downstream. At the $\frac{3}{70}$ revolution, HE1 is near the blade-2 leading edge and has occupied whole flow passage circumferentially at this span location.

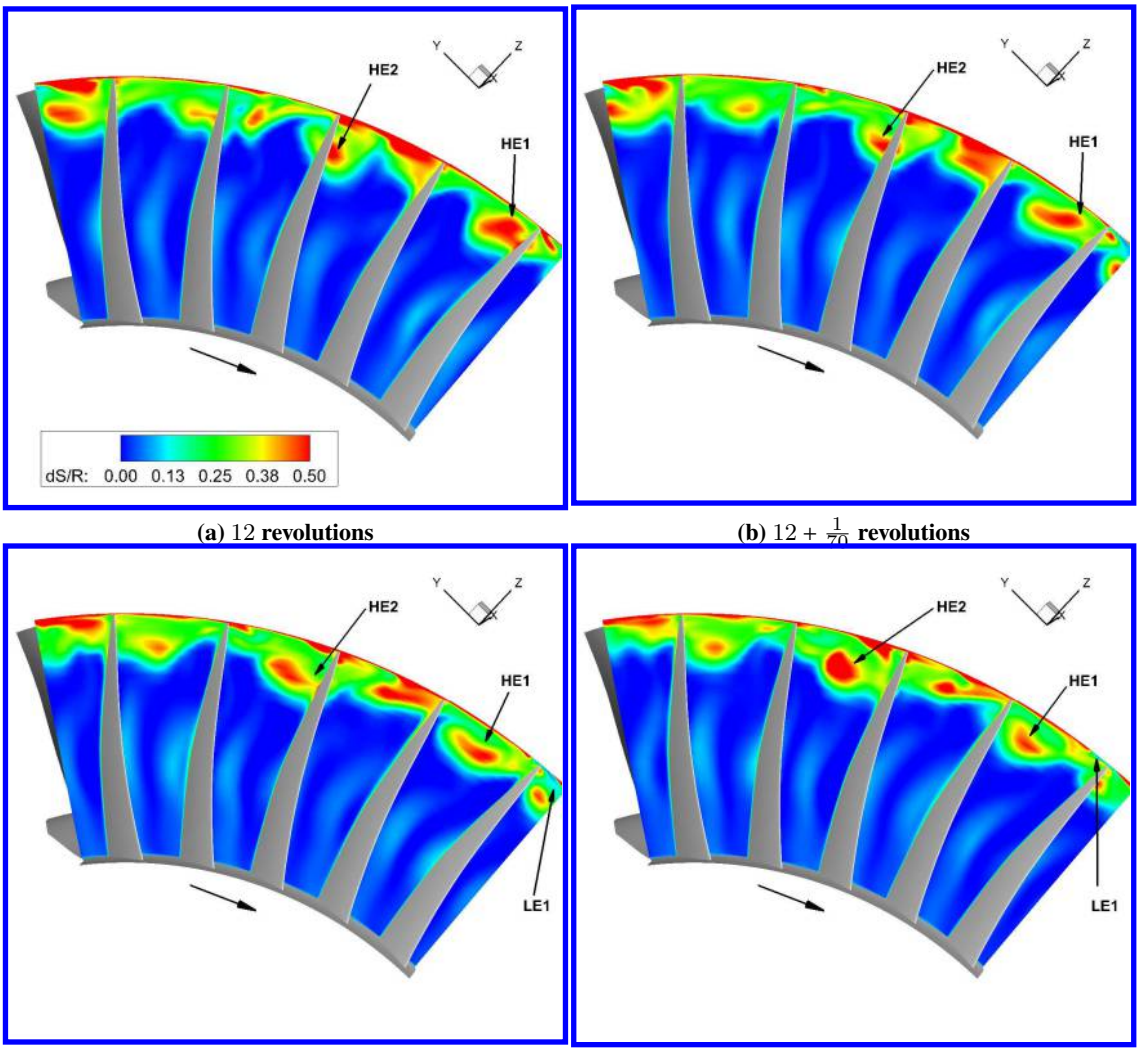

(a) 12 **revolutions**

(b) $12 + \frac{1}{70}$ **revolutions**

(c) $12 + \frac{2}{70}$ **revolutions**

(d) $12 + \frac{3}{70}$ **revolutions**

Figure 8 Entropy contours near the rotor leading edge

It is evident from the Fig. 8 that the tip vortex instability (i.e. HE1 and HE2) is traveling in the opposite direction of rotation. Apart from these high entropy regions, the low entropy region (LE1) is observed in the blade-1 tip clearance, Fig. 8 which is also counter rotating. It can also be seen that the high entropy regions are concentrated above the $80\,\%$ span location near the LE.

D. Total Pressure Ratio Radial Profile

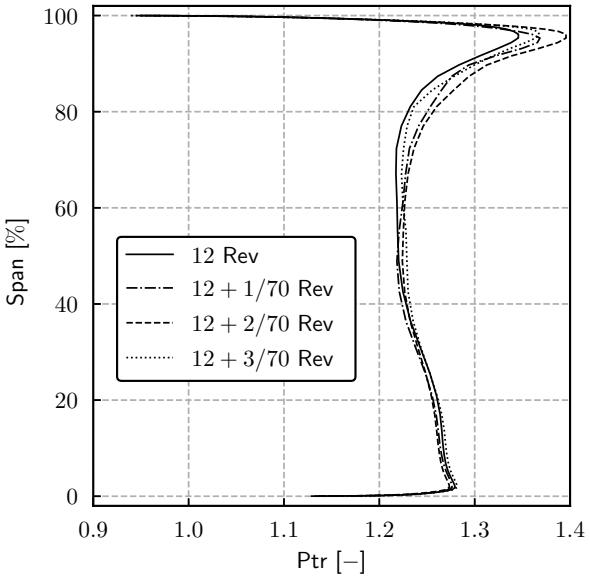

Figure 9 Variation in Total Pressure Ratio

Fig. 9 depicts circumferential mass flow rate averaged radial distribution of the total pressure ratio at various rotor revolutions. This pressure ratio is measured across the rotor outlet and IGV inlet. It can be seen that the pressure ratio variation is dominant near the $80\,\%$ and $96\,\%$ span locations. Below the $50\,\%$ span location, the variation in the total pressure ratio remains moderate. This also shows that the blade loading varies more above $80\,\%$ span location due to the tip flow instability.

VI. Conclusions

The predicted NSV frequency is in close agreement with the experimental result, with about $2.96\,\%$ under-prediction. The frequency analysis of the physical mass flow rate and blade surface static pressure shows that the NSV affects the global properties of the blade row whereas the vane passing frequency decays downstream in the present study. The experimental and numerical investigation have shown the NSV causes high amplitude blade vibration due to the high amplitude blade surface static pressure oscillation near the $85\,\%$ span location. The vortex shedding from the leading and trailing edge of the rotor blade is responsible for the NSV close to the 2^{nd} mode of blade vibration.

Acknowledgments

We would also like to thank the Center for Computational Science at the University of Miami, Coral Gables for providing computational resources. We thank GE for approval of publishing the NSV research under GUIde 4 program.

References

[1] Cumpsty, N. A., *Compressor Aerodynamics*, 2nd ed., Krieger Publishing Company, 2004.

[2] Baumgartner, M., Kameier, F., and Hourmouziadis, J., "Non-Engine Order Blade Vibration in a High Pressure Compressor," *Twelfth International Symposium on Airbreathing Engines*, Melbourne, Australia, 1995. URL `https://hal.archives-ouvertes.fr/hal-01353829`.

[3] Mailach, R., Lehmann, I., and Vogeler, K., "Rotating Instabilities in an Axial Compressor Originating From the Fluctuating Blade Tip Vortex," *Journal of Turbomachinery*, Vol. 123, No. 3, 2001.

[4] März, J., Hah, C., and Neise, W., "An Experimental and Numerical Investigation into the Mechanisms of Rotating Instability," *Journal of Turbomachinery*, Vol. 124, No. 3, 2002, pp. 367–374.

[5] Kielb, R. E., Barter, J. W., Thomas, J. P., and Hall, K. C., "Blade Excitation by Aerodynamic Instabilities: A Compressor Blade Study," 2003, pp. 399–406. doi:10.1115/gt2003-38634, URL http://dx.doi.org/10.1115/GT2003-38634, gT2003-38634.

[6] Thomassin, J., Vo, H. D., and Mureithi, N. W., "The tip clearance flow resonance behind axial compressor nonsynchronous vibration.(Author abstract)," *Journal of Turbomachinery*, Vol. 133, No. 4, 2011.

[7] Drolet, M., Vo, H. D., and Mureithi, N. W., "Effect of Tip Clearance on the Prediction of Nonsynchronous Vibrations in Axial Compressors," *Journal of Turbomachinery*, Vol. 135, No. 1, 2013.

[8] Im, H.-S., and Zha, G.-C., "Effects of Rotor Tip Clearance on Tip Clearance Flow Potentially Leading to NSV in an Axial Compressor," 2012, pp. 1383–1394. URL http://dx.doi.org/10.1115/GT2012-68148, gT2012-68148.

[9] Im, H., and Zha, G., "Investigation of Non-synchronous Vibration Mechanism for a High Speed Axial Compressor Using Delayed DES," AIAA SciTech Forum, American Institute of Aeronautics and Astronautics, 2014. doi:10.2514/6.2014-0789, URL https://doi.org/10.2514/6.2014-0789.

[10] Thomassin, J., Vo, H. D., and Mureithi, N. W., "Blade tip clearance flow and compressor nonsynchronous vibrations: the jet core feedback theory as the coupling mechanism.(Author abstract)(Report)," *Journal of Turbomachinery*, Vol. 131, No. 1, 2009.

[11] Zha, G.-C., and Bilgen, E., "Numerical Study of Three-Dimensional Flows Using Unfactored Upwind-Relaxation Sweeping Algorithm," *J. Comput. Phys.*, Vol. 125, No. 2, 1996, pp. 425–433. doi:10.1006/jcph.1996.0104, URL http://dx.doi.org/10.1006/jcph.1996.0104.

[12] Im, H., Chen, X., and Zha, G., "Simulation of 3D Multistage Axial Compressor Using a Fully Conservative Sliding Boundary Condition," 2011, pp. 1321–1330. doi:10.1115/imece2011-62049, URL http://dx.doi.org/10.1115/IMECE2011-62049, iMECE2011-62049.

[13] Allmaras, S., Johnson, F., and Spalart, P., "Modifications and Clarifications for the Implementation of the Spalart-Allmaras Turbulence Model," Seventh International Conference on Computational Fluid Dynamics (ICCFD7), 2012.

[14] Patel, P., and Zha, G., "Investigation of Mixed Micro-Compressor Casing Treatment using Non-Matching Mesh interface," 2019. GT2019-90977.

[15] Spalart, P. R., Jou, W.-H., Strelets, M., and Allmaras, S., "Comments on the Feasibility of LES for Wings, and on a Hybrid RANS/LES Approach," 1997.

[16] Spalart, P. R., Deck, S., Shur, M. L., Squires, K. D., Strelets, M. K., and Travin, A. K., "A New Version of Detached-eddy Simulation, Resistant to Ambiguous Grid Densities," *Theoretical and Computational Fluid Dynamics*, Vol. 20, No. 3, 2006, p. 181. doi:10.1007/s00162-006-0015-0, URL https://doi.org/10.1007/s00162-006-0015-0.

[17] Chaouat, B., "The State of the Art of Hybrid RANS/LES Modeling for the Simulation of Turbulent Flows," *Flow, Turbulence and Combustion*, Vol. 99, No. 2, 2017, pp. 279–327. doi:10.1007/s10494-017-9828-8, URL https://doi.org/10.1007/s10494-017-9828-8.

[18] Menter, F. R., Kuntz, M., and Bender, R., "A Scale-Adaptive Simulation Model for Turbulent Flow Predictions," Aerospace Sciences Meetings, American Institute of Aeronautics and Astronautics, 2003. doi:10.2514/6.2003-767, URL https://doi.org/10.2514/6.2003-767.

[19] Sagaut, P., Deck, S., and Terracol, M., *Multiscale and Multiresolution Approaches in Turbulence*, 2nd ed., London Imperial College Press, 2006.

[20] Menter, F. R., and Egorov, Y., "Revisiting the Turbulent Scale Equation," *IUTAM Symposium on One Hundred Years of Boundary Layer Research*, edited by G. E. A. Meier, K. R. Sreenivasan, and H.-J. Heinemann, Springer Netherlands, Dordrecht, 2006, pp. 279–290.

[21] Xu, C.-Y., Zhou, T., Wang, C.-L., and Sun, J.-H., "Applications of scale-adaptive simulation technique based on one-equation turbulence model," *Applied Mathematics and Mechanics (English Edition)*, Vol. 36, 2014, pp. 121–130. doi:10.1007/s10483-015-1898-9.

[22] Coder, J. G., "A Scale-Adaptive Variant of the Spalart-Allmaras Eddy-Viscosity Model," AIAA AVIATION Forum, American Institute of Aeronautics and Astronautics, 2015. doi:10.2514/6.2015-2462, URL https://doi.org/10.2514/6.2015-2462.

[23] Patel, P., Yang, Y., and Zha, G., "Scale Adaptive Simulation of stalled NACA 0012 airfoil using high order schemes," *AIAA Aviation 2019 Forum*, 2019. doi:10.2514/6.2019-3527, URL https://arc.aiaa.org/doi/abs/10.2514/6.2019-3527.

[24] Katopodes, N., *Free-Surface Flow: Environmental Fluid Mechanics*, 1st ed., Butterworth-Heinemann, 2018.

[25] Menter, F. R., and Egorov, Y., "The Scale-Adaptive Simulation Method for Unsteady Turbulent Flow Predictions. Part 1: Theory and Model Description," *Flow, Turbulence and Combustion*, Vol. 85, No. 1, 2010, pp. 113–138. doi:10.1007/s10494-010-9264-5, URL https://doi.org/10.1007/s10494-010-9264-5.

[26] Im, H.-S., and Zha, G.-C., "Simulation of Non-Synchronous Blade Vibration of an Axial Compressor Using a Fully Coupled Fluid/Structure Interaction," 2012, pp. 1395–1407. doi:10.1115/gt2012-68150, URL http://dx.doi.org/10.1115/GT2012-68150, gT2012-68150.

[27] Im, H., Chen, X., and Zha, G., "Detached Eddy Simulation of Unsteady Stall Flows of a Full Annulus Transonic Rotor," *Journal of Propulsion and Power*, Vol. 28, No. 4, 2011. doi:10.2514/1.B34395.

[28] Zha, G.-C., Shen, Y., and Wang, B., "An improved low diffusion E-CUSP upwind scheme," *Computers & Fluids*, Vol. 48, No. 1, 2011, pp. 214 – 220. doi:https://doi.org/10.1016/j.compfluid.2011.03.012, URL http://www.sciencedirect.com/science/article/pii/S0045793011000983.

[29] Antony, J., "Time dependent calculations using multigrid, with applications to unsteady flows past airfoils and wings," Fluid Dynamics and Co-located Conferences, American Institute of Aeronautics and Astronautics, 2018. doi:10.2514/6.1991-1596, URL https://doi.org/10.2514/6.1991-1596.

[30] Wang, B., Hu, Z., and Zha, G., "A General Sub-Domain Boundary Mapping Procedure For Structured Grid CFD Parallel Computation," *AIAA Journal of Aerospace Computing, Information, and Communication*, Vol. 5, 2008, pp. 425–447.